Surface magnetic activity of the fast-rotating G5-giant IN Comae, central star of the faint planetary nebula LoTr 5[⋆]

Zs. Kővári[1], K. G. Strassmeier[2], K. Oláh[1], L. Kriskovics[1], K. Vida[1], T. A. Carroll[2], T. Granzer[2], I. Ilyin[2], J. Jurcsik[1], E. Kővári[3], and M. Weber[2]

[1] Konkoly Observatory, Research Centre for Astronomy and Earth Sciences, Hungarian Academy of Sciences, Konkoly Thege út 15-17., H-1121, Budapest, Hungary; e-mail: `kovari.zsolt@csfk.mta.hu`
[2] Leibniz-Institute for Astrophysics Potsdam (AIP), An der Sternwarte 16, D-14482 Potsdam, Germany
[3] Eötvös University, Department of Astronomy, Pf. 32., H-1518, Budapest, Hungary

ABSTRACT

Context. On the asymptotic giant branch, low to intermediate mass stars blow away their outer envelopes, forming planetary nebulae. Dynamic interaction between the planetary nebula and its central progenitor is poorly understood. The interaction is even more complex when the central object is a binary star with a magnetically active component, like it is the case for the target in this paper.
Aims. We aim to quantify the stellar surface activity of the cool binary component of IN Com and aim to explain its origin. In general, we need a better understanding of how central binary stars in planetary nebulae evolve and how this evolution could develop such magnetically active stars like IN Com.
Methods. We present a time-series of 13 consecutive Doppler images covering six months in 2017 and use it to measure the surface differential rotation with a cross-correlation method. Hitherto unpublished high-precision photometric data from between 1989 to 2017 are presented. We apply Fourier-transformation based frequency analysis to both photometry and spectra. Very high resolution ($R \approx 200,000$) spectra are used to update IN Com's astrophysical parameters by means of spectral synthesis.
Results. Our time-series Doppler images show cool and warm spots coexisting with an average surface temperature contrast of -1000 K and $+300$ K with respect to the effective temperature. Approximately 8% of the stellar surface is covered with cool spots and $\approx$3% with warm spots. A consistent cool polar spot is seen in all images. The average lifetime of the cool spots is not much more than a few stellar rotations (one month), while the warm spots appear to live longer (3 months) and are mostly confined to high latitudes. We found anti-solar surface differential rotation with a shear coefficient of $\alpha = -0.026 \pm 0.005$ suggesting an equatorial rotation period of 5.973 ± 0.008 d. We reconfirm the 5.9-day rotation period of the cool star from photometry, radial velocities, and Hα line-profile variations. A long-term V-brightness variation with a likely period of 7.2 yr is also found. It appears in phase with the orbital radial velocity of the binary system in the sense brightest at highest velocity and faintest at lowest velocity, that is, at the two phases of quadrature. We redetermine [Ba/Fe], [Y/Fe] and [Sr/Fe] ratios and confirm the overabundance of these s-process elements in the atmosphere of IN Com.

Key words. stars: activity – stars: imaging – stars: late-type – stars: starspots – stars: individual: IN Com

1. Introduction

Undergoing the asymptotic giant branch (AGB) evolution phase, low to intermediate mass stars blow away their outer envelopes, forming planetary nebulae that will be ionized by the developing white dwarfs in their center. However, interaction between the planetary nebula and its central progenitor is far from understood. The scheme is even more complicated, when the central object is a binary star, which may be the majority (e.g., De Marco et al. 2004; Jones & Boffin 2017). When the binary system is embedded in a common envelope, the components evolve together, as initially proposed by Paczyński (1976). Inside the envelope the stellar cores spiral together and finally they may merge, forming a fast-rotating giant star, such as FK Comae stars (for a recent overview of binary mergers see the contribution by Ph.

Podsiadlowski in González Martínez-País et al. 2014). However, if the envelope material is ejected before merging, the binary evolution may end up in a system involving a white dwarf and a main sequence companion. In this case some of the ejected nebular material is captured by the companion, yielding cataclysmic variability, while the accretion gradually spins up the accreting star. In addition, a powerful magnetic dynamo can also develop, since the common envelope is largely convective and supposed to rotate differentially (Tout & Regős 2003). However, the theory of common envelope evolution is extremely complex, involving different physical processes (e.g., ejection, accretion, spiralling, magnetic braking) on different time-scales (thermal, dynamical, hydrodynamical, magneto-hydrodynamical, etc.), therefore a self-consistent, all-comprehensive treatment is still not feasible (cf. Podsiadlowski 2001).

In this paper we revisit one of our former Doppler imaging targets, IN Comae (=HD 112313, Strassmeier et al. 1997b, hereafter Paper 1), the central object of the faint planetary nebula LoTr 5 (Longmore & Tritton 1980). The system consists of a white dwarf and a giant G-star, which is evident from the com-

posite IUE spectra (Feibelman & Kaler 1983). Actually, the central object is a long-period ($P_{orb} \approx 2700\,d \approx 7.4\,yr$) binary system, consisting of a rapidly rotating magnetically active G5 giant ($v \sin i = 67\,kms^{-1}$) and a hot ($T_{eff} \approx 150\,000\,K$) subdwarf companion (cf. Jones et al. 2017, and their references). It was even suggested that the G5 component had a close companion, forming a hierarchical triple system (Jasniewicz et al. 1987; Malasan et al. 1991). However, this option has recently been disproved by Van Winckel et al. (2014), who suggested that either the white dwarf (or hot subdwarf) formed a close binary together with a yet undiscovered star of some 2–3 $M_{\odot}$, or alternatively the orbital plane was not coplanar with the waist of the bipolar nebula. The cool star was found to be barium-rich (Thévenin & Jasniewicz 1997) as a consequence of contamination by s-process elements from the AGB progenitor envelope (cf. Bisterzo et al. 2011), supporting the presumption of spinning-up of the cool component by accreting the ejected envelope material.

Rotational and orbital period determinations of IN Com in the past yielded misinterpretations and even contradictory results. As fundamental period 5.9-day was reported by Noskova (1989), which was attributed to rotation of the G5 giant (see Paper 1). However, Malasan et al. (1991) argued for 1.2-day as the most prominent photometric signal (i.e., the $1 - f$ alias of 5.9 days), and also for 1.75 days, based on radial velocity measurements, as a possible orbital period of the assumed close binary. Jasniewicz et al. (1994) could not confirm this binary orbit, but they claimed that 1.2-day was indeed correct. After a revision, however, Jasniewicz et al. (1996) found the 5.9-day period as more realistic. Oddly, Kuczawska & Mikolajewski (1993) found an even shorter period of 0.25 days, which, however, has not been confirmed ever since. Over and above, the radial velocity measurements in Paper 1 did not support the close binary hypothesis. Only recently, Jones et al. (2017) have updated the first reliable orbital motion detection by Van Winckel et al. (2014) and proposed an orbital period of 2717±63 days (≈7.4 years) for the G5 star.

IN Com has been observed in X-rays by *XMM-Newton* with all three European Photon Imaging Cameras (EPIC) on 6 June 2002, and by *Chandra* on 4 December 2002 (Montez et al. 2010). Spectral fitting shows that the X-ray emission is characterized by two components at about 0.65 keV (both *XMM-Newton* and *Chandra*) and at 2.27 and 3.49 keV (*XMM-Newton* and *Chandra*, respectively), while the X-ray luminosity was measured as $\log L_X \approx 30\,erg\,s^{-1}$. Guerrero (2012) fitted the *XMM-Newton* EPIC planetary nebula spectrum with $8 \times 10^{30}\,erg\,s^{-1}$ at 0.61 and 3.1 keV, and constructed a spectral energy distribution model from the *XMM-Newton* data, the available *IUE* spectra, and ground based optical and near-infrared photometry. The non-local thermodynamic equilibrium (non-LTE) model showed good agreement with a contribution from a supposed G5 III companion star. It seems, that the X-ray emission dominantly originates from the corona of the magnetically active late-type component of the binary (see Montez et al. 2010, for details).

Our study may contribute in moving towards a better understanding how central binary stars in planetary nebulae evolve and how this evolution could develop such fast-rotating magnetically active stars like IN Com. The paper is organized as follows. In Sect. 2 we present the photometric and spectroscopic observations. In Sect. 3 we provide updated astrophysical parameters for IN Com and present a time-series Doppler imaging study. With that we analyze the spot evolution and measure the surface differential rotation. In Sect. 4 we study the photometric and spectroscopic variability of the IN Com system, while in Sect. 5 the

Hα behaviour is examined. The results are summarized and discussed in Sect. 6.

2. Observations

2.1. Photometry

Most of the photometric observations were obtained with the T6 and T7 ('Wolfgang' and 'Amadeus', respectively) 0.75-m automatic photoelectric telescopes (APTs) located at Fairborn Observatory in southern Arizona (Strassmeier et al. 1997a), operated by AIP (Granzer et al. 2001). Altogether 1364 data points were observed in Johnson V (T6) and 943 in Strömgren y (T7) colours between February 1996–June 2017 (JD 2,450,117–2,457,911). Besides, 643 Johnson V observations were collected with the 1-m RCC telescope of Konkoly Observatory, Budapest, located at Piszkéstető mountain station, Hungary, between January 1989–June 1993 (JD 2,447,530–2,449,141). The old photometric data from the literature completed with the new, yet unpublished V and y observations are plotted together in Sect. 4 in the top panel of Fig. 6.

2.2. Spectroscopy

Spectroscopic observations were carried out with the 1.2-m STELLA-II telescope of the STELLA robotic observatory (Strassmeier et al. 2010) located at the Izaña Observatory in Tenerife, Spain. It is equipped with the fibre-fed, fixed-format STELLA Echelle Spectrograph (SES) providing an average spectral resolution of $R = 55\,000$. Altogether 230 high-resolution echelle spectra were recorded between January 26 and June 23, 2017. The spectra cover the 3900–8800 Å wavelength range without gaps. Further details on the performance of the system and the data-reduction procedure can be found in Weber et al. (2008, 2012) and Weber & Strassmeier (2011). The average signal-to-noise ratio (S/N) of the spectra is 140:1. Table A.1 in the Appendix summarizes the division of the spectra into 12 independent subsets (dubbed S01–S12) which are used for Doppler imaging.

In addition, 20 ultra-high resolution ($R = 200\,000$) spectra were collected during March 03–15, 2017 with the 1.8-m Vatican Advanced Technology Telescope (VATT) fiber linked to the Potsdam Echelle Polarimetric and Spectroscopic Instrument (PEPSI) at the nearby Large Binocular Telescope (LBT). PEPSI's characteristics and performance were described by Strassmeier et al. (2015, 2018). With cross disperser (CD) III in the blue arm and CD V in the red arm the set-up provided a wavelength coverage of 4800–5440 Å and 6280–7410 Å, respectively. The 90-min exposures gave typical S/N of 100:1 for the red and 50:1 for the blue wavelength regions. This data set is used primarily to refine some of the fundamental astrophysical parameters of IN Com (see Sect. 3.1). The log for these observations is given in Table A.2 in the Appendix.

3. Doppler imaging

3.1. Adopted stellar parameters

The effective temperature, the surface gravity, the metallicity, and the microturbulence velocity are re-examined by applying the spectrum-synthesis code SME (Piskunov & Valenti 2017) to the ultra-high resolution PEPSI spectra. Our synthesis is based on MARCS model atmospheres (Gustafsson et al. 2008) and assuming local thermodynamic equilibrium (LTE). Atomic param-

eters are taken from the Vienna Atomic Line Database (VALD, Kupka et al. 1999). For the spectrum synthesis we used the 4800–5441 Å and 6278–7419 Å wavelength ranges. SME is applied for all single PEPSI spectra and the individual results are combined in order to estimate their error bars. This way we get T_{eff}= 5400 ± 100 K, log g=2.6 ± 0.1, [Fe/H]=−0.10 ± 0.05 and ξ_{mic}=2.0 ± 0.4 km s^{-1} for the effective temperature, surface gravity, metallicity and microturbulence, respectively. We note that our temperature and surface gravity values are in good agreement with the recent result by Aller et al. (2018). The radial-tangential macroturbulence dispersion of ≈7 km s^{-1} is estimated according to Gray (1981) and Gray & Toner (1986). SME was used to measure the Ba, Y and Sr abundances (cf. Thévenin & Jasniewicz 1997) as well. For the abundance fits we kept all of the other redetermined astrophysical parameters fixed. We note that for the Ba line fit we take the average of 40 high quality STELLA spectra since the spectral gap between the blue and red arms of the PEPSI data highly overlaps with the 5519–6694 Å region of the 31 neutral and singly ionized barium lines taken from VALD. The new astrophysical data of IN Com are summarized in Table 1.

Table 1. The astrophysical properties of IN Com

Parameter	Value
Spectral type	G5 III
Gaia distance [pc]	506 ± 12
V_{br} [mag]	8.69 ± 0.03
$(B - V)_{\mathrm{HIP}}$ [mag]	0.835 ± 0.004
M_{bol} [mag]	0.01 ± 0.08
Luminosity [$L_{\odot}$]	78 ± 6
log g [cgs]	2.6 ± 0.1
T_{eff} [K]	5400 ± 100
$v \sin i$ [km s^{-1}]	67.0 ± 1.5
Photometric period [d]	5.934 ± 0.001
Equatorial rotation period [d]	5.973 ± 0.008
Differential rotation coefficient	−0.026 ± 0.005
Inclination [°]	45 ± 15
Radius [$R_{\odot}$]	$11.1^{+5.0}_{-2.2}$
Mass [$M_{\odot}$]	1.8 ± 0.4
Microturbulence [km s^{-1}]	2.0 ± 0.4
Macroturbulence [km s^{-1}]	7.0 (adopted)
Metallicity [Fe/H]	−0.10 ± 0.05
Barium/iron ratio [Ba/Fe]	0.85 ± 0.25
Yttrium/iron ratio [Y/Fe]	0.27 ± 0.12
Strontium/iron ratio [Sr/Fe]	≳ 1.0

The projected equatorial velocity of 67±1.5 km s^{-1} (Paper 1, but see also Van Winckel et al. 2014) and a 45±15° inclination (cf. Paper 1) together with the equatorial rotation period of 5.973 d (cf. Sect. 4.2) yields a stellar radius of $11^{+5.0}_{-2.2}$R$_{\odot}$. Together with T_{eff}=5400±100 K this radius is consistent with the G5 III classification in the literature.

The new *Gaia* DR-2 parallax of 1.977±0.046 mas (Gaia Collaboration et al. 2018) yields a distance of 506±12 pc for IN Com. The brightest ever observed V magnitude of 8$^{\mathrm{m}}$69 ± 0$^{\mathrm{m}}$03 (see later Fig. 7), while neglecting any interstellar and circumstellar extinction (cf Ciardullo et al. 1999), results in an absolute magnitude M_V=0$^{\mathrm{m}}$17 ± 0$^{\mathrm{m}}$08. This, together with a bolometric correction for a G5 giant of $BC = -0^{\mathrm{m}}163$ taken from Flower (1996) gives a bolometric magnitude of M_{bol}=0$^{\mathrm{m}}$01 ± 0$^{\mathrm{m}}$08, and thus a luminosity of $L = 78 ± 6 L_{\odot}$ in fair agreement with the value just from the Stefan-Boltzmann law, but with a much smaller error bar. Also, taking above radius and our measured gravity the stellar mass is ≈ 1.8 ± 0.4 M$_{\odot}$.

3.2. Definition of data subsets

The spectroscopic data used for the Doppler-imaging (DI) process are all from the first half of 2017 and are distributed fairly uniformly over the five-months STELLA run. In spite of the relatively short rotation period of 5.9 d, we still got satisfactory phase coverage with between 8 and 13 spectra per image for 12 subsequent intervals of typically one stellar rotation each. An additional subset can be formed from the available PEPSI spectra, with a pretty dense phase coverage. Table 2 summarizes the timely distribution of the 13 data subsets (dubbed S01–S12 and P01 for the PEPSI spectra) while Tables A.1 and A.2 in the Appendix record the observing logs for the STELLA and the PEPSI spectra, respectively.

3.3. Image reconstruction with iMap

Our Doppler-imaging code *iMap* (Carroll et al. 2012) performs a temperature inversion for a number of photospheric line profiles simultaneously. For the inversions 20 suitable absorption lines were selected from the 5000–6750 Å wavelength range (for the selection criteria see Künstler et al. 2015). Each spectral line is modeled individually and locally, then being disk-integrated and in the final step all disk-integrated line regions are averaged to obtain a mean theoretical profile. These mean profiles are then compared with each observed mean profile (for more details see Sect. 3 in Carroll et al. 2012). For the preparation of the observed mean profile we proceed with a simple S/N-weighted averaging to increase the overall S/N by a factor of ≈4. *iMap* calculates the local line profiles by solving the radiative transfer with the help of an artificial neural network (Carroll et al. 2008). Atomic parameters are taken from the VALD database (Kupka et al. 1999). Model atmospheres are taken from Castelli & Kurucz (2004) and are interpolated for each desired temperature, gravity and metallicity. Due to the high CPU demand only LTE radiative transfer is used instead of spherical non-LTE model atmospheres.

For the surface reconstruction *iMap* uses an iterative regularization based on a Landweber algorithm (Carroll et al. 2012). According to our tests (see Appendix A in Carroll et al. 2012) the iterative regularization has been proven to converge always on the same image solution. Therefore, no additional constraints are imposed for the image reconstruction. The surface element resolution is set to 5° × 5°.

3.4. Results: spot morphology and evolution

The resulting 13 time-series Doppler reconstructions of IN Com for 2017 (12 maps for the STELLA observations and one for the PEPSI spectra) are plotted in Figs. 1, 2 and 3. The line-profile fits are given in the Appendix in Figs. A.1, A.2 and A.3, respectively. The overall surface structure characteristics is reminiscent of the first and so far only Doppler image from 1994 (see Paper I), revealing a cool spot on the visible pole, cool spots at low to high latitudes and even a few hot spots mostly at mid-latitudes. The spot temperatures range from the coolest ≈3600 K up to ≈5800 K, i.e., hotter by 400 K than the unspotted photosphere of 5400 K. Hot spots are often claimed to be artifact of the imperfect reconstruction. Lindborg et al. (2014, see their Fig. 3) have demonstrated that such artifacts are usually the result of extremely sparse phase coverage. However, regarding the recon-
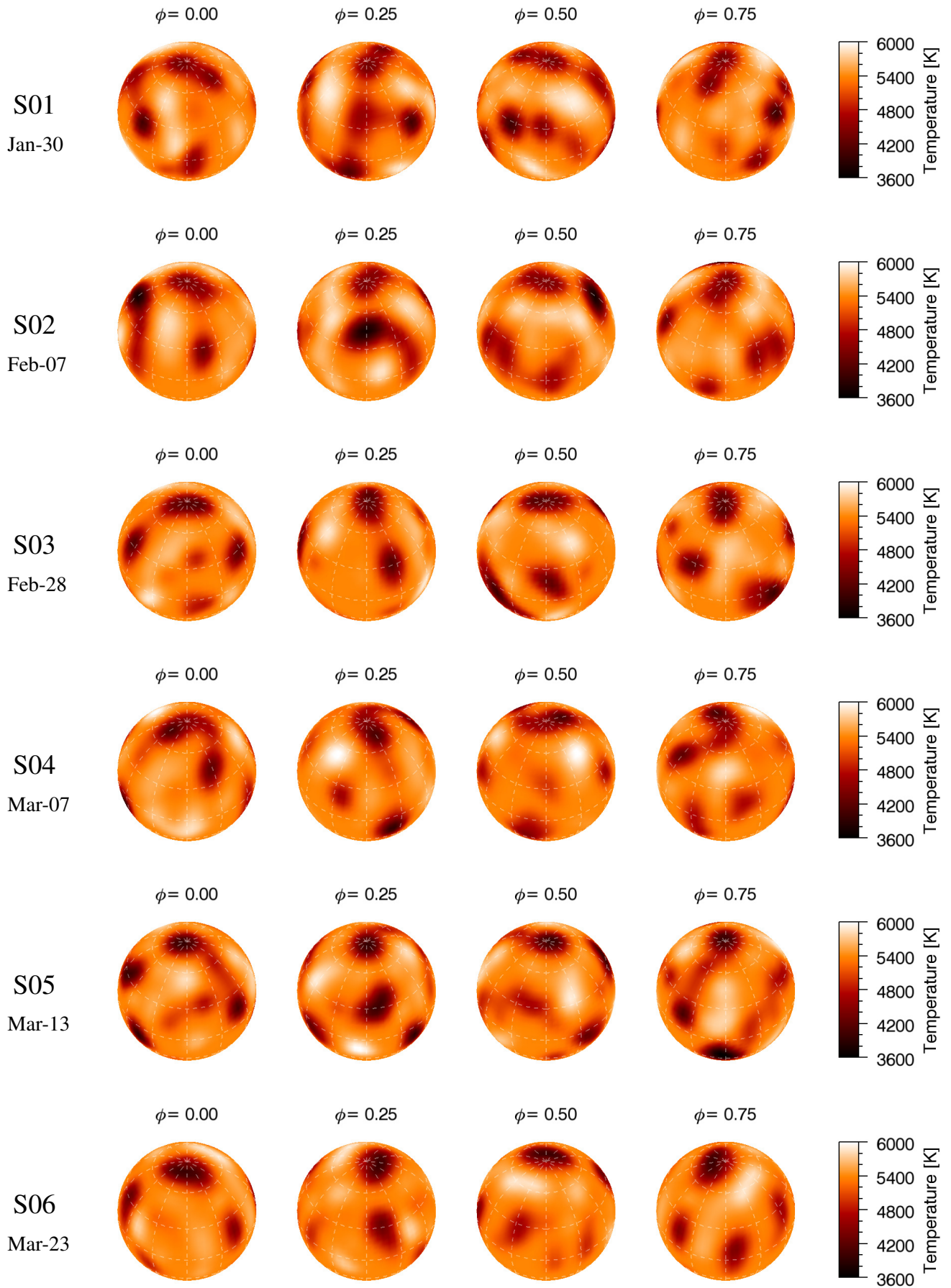
Fig. 1. Doppler images of IN Com for STELLA data sets S01–S06. The corresponding mid-UT dates (2017+) are indicated below the names of the maps.
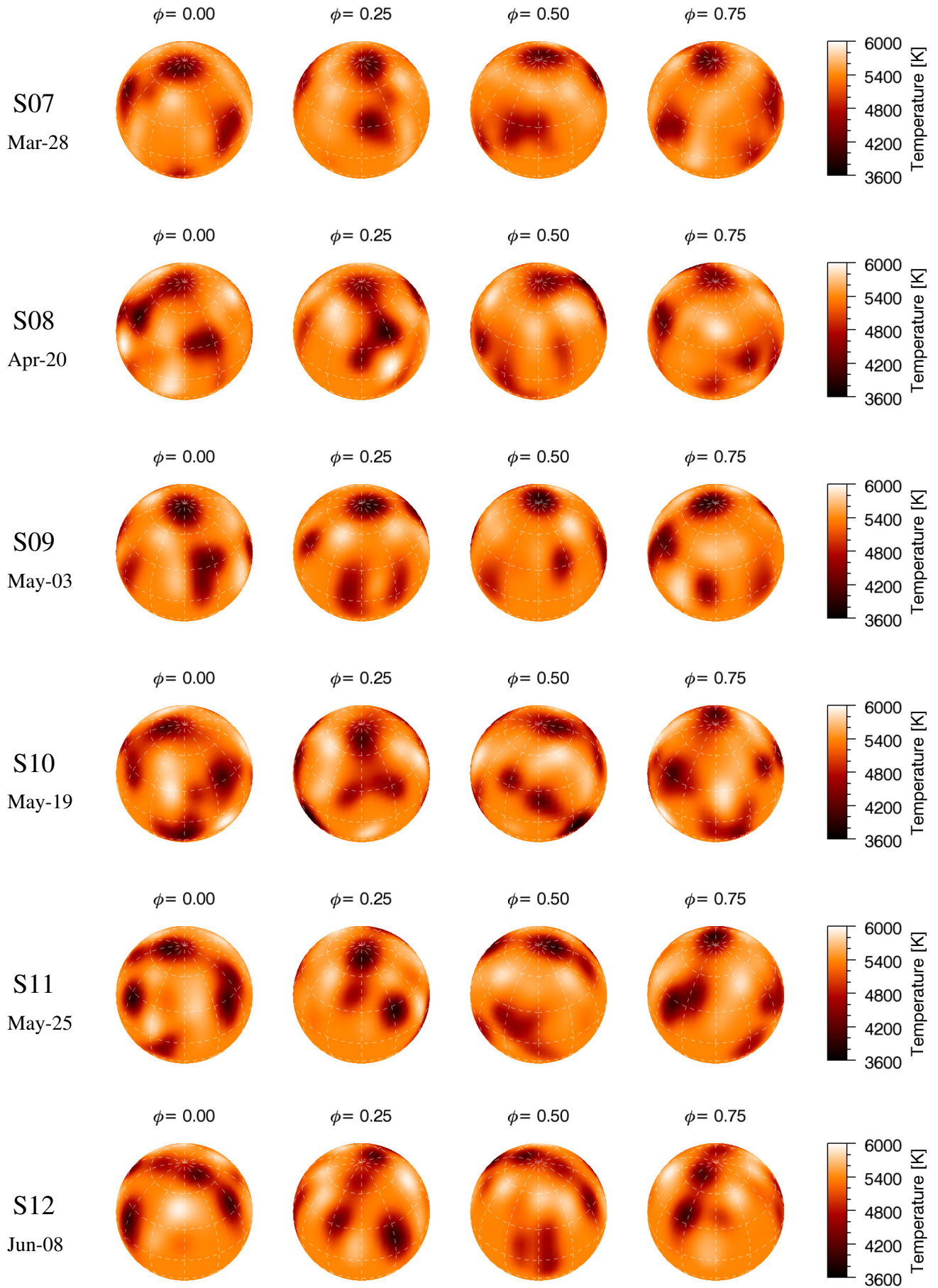
Fig. 2. Doppler images for STELLA data sets S07–S12. The corresponding mid-UT dates (2017+) are indicated below the names of the maps.

Table 2. Temporal distribution of the subsequent datasets for each individual Doppler image

Data subset	Mid-HJD 2 450 000+	Mid-date 2017+	Number of spectra	Data range in days	Data range in P_{rot}
S01	7784.490	Jan-30	8	6.910	1.164
S02	7791.670	Feb-07	11	5.091	0.858
S03	7813.465	Feb-28	13	7.984	1.345
S04	7819.742	Mar-07	11	4.967	0.837
P01	7823.892	Mar-11	18	8.141	1.372
S05	7826.080	Mar-13	13	5.230	0.881
S06	7835.673	Mar-23	9	4.732	0.797
S07	7841.438	Mar-28	13	5.050	0.851
S08	7864.277	Apr-20	9	8.166	1.376
S09	7877.389	May-03	9	10.149	1.710
S10	7892.854	May-19	11	5.214	0.879
S11	7898.804	May-25	10	5.175	0.872
S12	7912.724	Jun-08	9	5.135	0.865
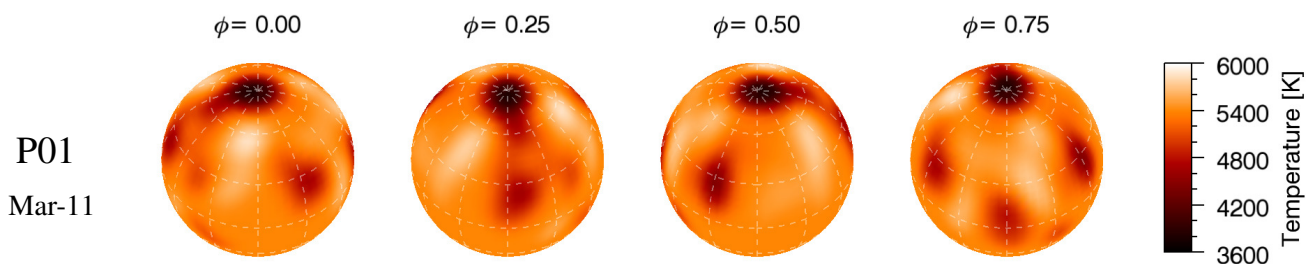
Fig. 3. Doppler image for the PEPSI@VATT spectra. The corresponding mid-UT date is 2017-03-11, which falls just between the dates of S04 and S05 maps shown in Fig. 1.

structions as a time series we observe that subsequent maps reveal quite similar features (cool as well as hot spots) from totally independent data. Moreover, insufficient phase sampling would introduce artificial (hot as well as cool) features at different locations from one Doppler reconstruction to the next, i.e., usually around phases where the largest phase gaps appear. However, our datasets are well sampled, and their largest gaps (usually below 0.15-0.17 phase fraction, i.e. still not very large) appear randomly along the rotation phase, therefore we do not expect such artificial hot (and cool) features at similar locations over the 13 individual Doppler reconstructions. Note especially the P01 PEPSI-map shown in Fig. 3, which falls between the S04 and S05 STELLA-maps and despite the different observing facilities and independent data the recovered surface features show remarkable resemblance. This confirms not only the reliability of the reconstructed features but also the steadiness and robustness of *iMap*. The polar spot seems to be the most permanent feature over the time range, while at lower latitudes the spotted surface is more variable, still, the dominant features can be tracked from one map to the next. Finally, we note that in some maps strong features are seen also below the equator, despite that Doppler imaging is less powerful when reconstructing the less visible hemisphere. We assume, however, that such a feature is most likely real when it reappears on consecutive Doppler reconstructions (see S03-S04-S05 and S10-S11), although the shape, size or contrast of these features may be loose.

The first reconstruction in the time series (S01) reveals an elongated polar feature of ≈4800 K together with several lower latitude nearly circular spots of ≈4000−5000 K with typically 10° diameter. The brightest feature of ≈5800 K is centered at phase ϕ=0.4 at high (≈50°) latitude. A faint cool spot at ϕ=0.25

is becoming the most prominent cool feature for the next map (S02), while the hot spot as well as the other cool spots are getting less contrasted. For the next map (S03) the polar spot is getting cooler and more compact, while other cool spots are shrinking by ≈30-60%. The only exception is the new cool feature at the lower hemisphere, just at the border of visibility. We note that the bright spot at ϕ=0.4 is permanently visible. For the next (S04) map the cool spots are becoming fainter, however, the bright spot at ϕ=0.4 is hotter. S05, the fifth map reveals an emerging new cool spot at ϕ≈0.3, while the polar spot has become more compact and contrasted. In the next map (S06) the progeny of the new spot, as well as the other cool and bright features, become smaller and/or less contrasted. This continues in S07 map, where the hot features nearly vanish. Traces of new flux emergence are seen in S08 with a new spot at ϕ≈0.2. Also, bright features appear again, in particular the well-known one at ϕ=0.4. In the next map (S09) the polar spot is getting more prominent while the newly emerged spot at ϕ≈0.2 fades and splits into two subspots. The high latitude bright spot at ϕ=0.4 is still detectible. In the tenth map (S10) a new cool spot group emerged at ϕ≈0.5, and is getting less contrasted and shifted towards the covered pole in the S11 map. Also, the formerly vanishing spot around 0.2 phase appears now strengthened. This continues during our last reconstruction (S12), where the polar spot is shrinking and also displacing. Permanent rearrangements are taking place, e.g. the spot group in S11 at ϕ≈0.9 is getting smaller in size and cooler. Note also, that the high latitude warm (≈5600−5900 K) features are still present.

For each map the overall surface temperature is obtained by averaging the temperature values pixel by pixel over the stellar surface. However, tracing individual spots from one map to the
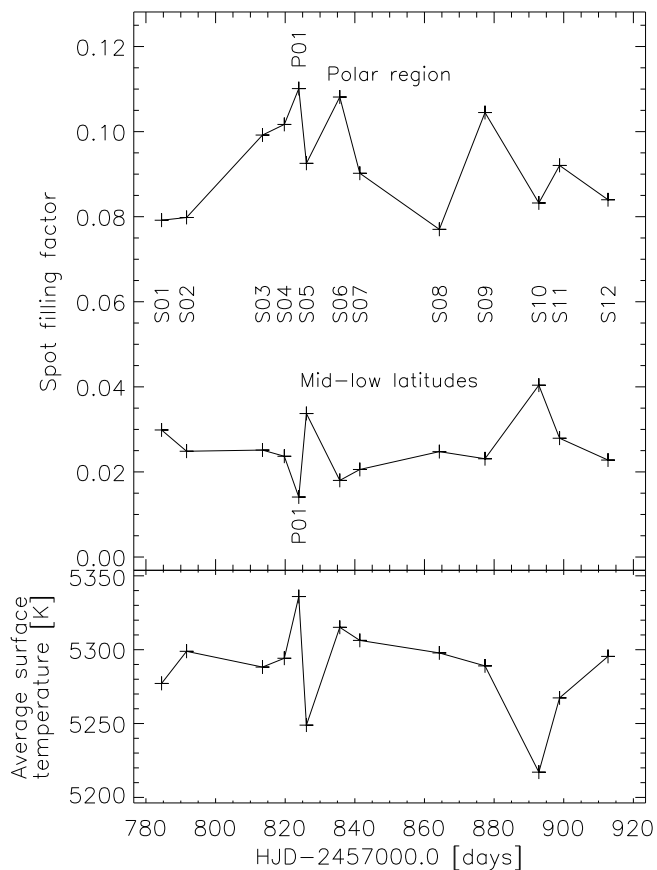
Fig. 4. Time variation of the spot filling factor (top panel) and the integrated surface temperature (bottom panel) of IN Com derived from the time-sereies Doppler images shown in Figs. 1, 2 and 3. In the upper panel the spot filling factors are shown for the polar region and for the mid-to-low latitudes separately; see the top and the bottom curves, respectively. The different Doppler reconstructions are identified by their serial numbers.

next is hampered by the rapid spot rearrangements and/or the imperfect phase coverages. Instead, we split the surface into two parts above and below 65°, this way ranking the spots to be either polar or low-to-mid latitude spots. We measure the time variation of both surface partitions by deriving the spot filling factor values. In Fig. 4 we plot the time variation of the average temperature from surface integration as well as the spot filling factors. The diagrams indicate two epochs at HJD 2 457 826 (S05) and HJD 2 457 893 (S10), when the average temperature decreased by ≈50 K, simultaneously with a small drop of the filling factor at the pole, but a significant increase of ≈40% at mid-low latitudes. According to the maps, these two events may indicate significant spot rearrangements, when new fluxes emerge. On the other hand, individual spot evolutions imply that the average spot lifetime should be of the order of a month.

3.5. Surface differential rotation

Tracking short term spot migrations is among the usual methods to study stellar surface differential rotation from Doppler imaging (Donati & Collier Cameron 1997). In this paper, we apply the program ACCORD (Kővári et al. 2015, and references therein) and perform a time-series cross-correlation analysis
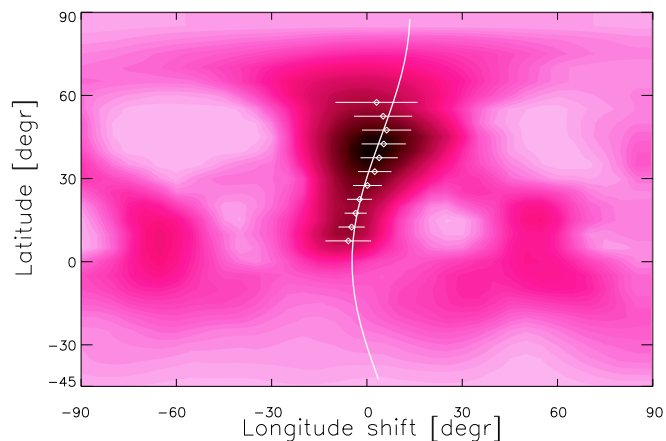

Fig. 5. Average cross-correlation map for IN Com showing anti-solar surface differential rotation. The best correlated dark regions are fitted by Gaussian curves in 5° bins. Gaussian peaks are indicated by dots, the corresponding Gaussian widths by horizontal lines. The best fit differential rotation law suggests an equatorial period of $P_{eq} = 5.973$ d and a surface shear coefficient of $\alpha = -0.026$.

from the 12 Doppler images obtained for the STELLA observations (for the sake of data homogeneity we excluded the P01 map from this analysis). It provides 11 consecutive cross-correlation function (ccf) maps which are combined into an average correlation map. Its 2D correlation pattern is then fitted with a quadratic differential-rotation law in the usual (solar) form of $\Omega(\beta) = \Omega_{eq}(1 - \alpha \sin^2 \beta)$, where $\Omega(\beta)$ is the angular velocity at latitude β, Ω_{eq} the angular velocity at the equator, while $\alpha = (\Omega_{eq} - \Omega_{pole})/\Omega_{eq}$ is the relative angular velocity difference between the equator and the pole, i.e. the surface shear coefficient.

The resulting correlation pattern for IN Com is shown in Fig. 5. It indicates anti-solar surface differential rotation, i.e., the equator rotates slower than the polar latitudes. The most well correlated dark regions are fitted with Gaussian curves in 5° bins. The Gaussian peaks are indicated in Fig. 5. The best fit to these peaks gave $\Omega_{eq} = 60.28 \pm 0.08$ °/d or an equivalent equatorial period of $P_{eq} = 5.973 \pm 0.008$ d with a shear coefficient of $\alpha = -0.026 \pm 0.005$. This yields a lap time of 230 d needed by the polar regions to lap the equator by one full rotation.

4. Variability of the IN Comae system

4.1. Orbital photometric modulation

Fig. 6 presents photometric data of IN Com for the past 30+ years. To support a long-period search our new photometric data are combined with the published observations from Paper I and augmented with observations from the All Sky Automated Survey (ASAS) database (Pojmanski 2002). The (binned) Super-WASP data in Aller et al. (2018) could not be used due to missing bandpass transformations but overlap with part of the ASAS data anyway. For the period determination, we apply the Fourier-transformation based frequency analyzer code MuFrAn (Csubry & Kolláth 2004). In the top panel of Fig. 6, we show the best fit to the full photometric data set with a sinusoid of a period of 2639 d (≈7.2 yr), which has an uncertainty of about 200 d. The sine-wave fits well the first two well-observed cycles and does not contradict with the later, sparse data.

The photometric cycle of 2639 d is in surprising agreement with the recently proposed orbital period of 2717±63 d (Jones
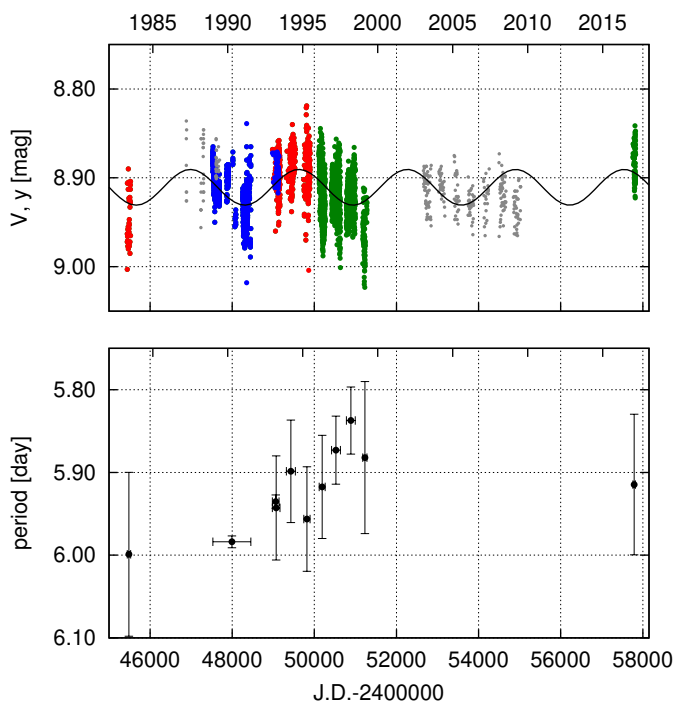
Fig. 6. Top: long-term photometric *V* and *y* data of IN Com. Different colors mean different sources of observations; green: data from T6 and T7 APTs, blue: observations from the Hungarian 1-m RCC telescope, red: literary data (mostly from Paper 1) which are used for seasonal period determination, grey: literary data+ASAS data which are not suitable for seasonal period determination. The sine-wave fit by black solid line represents the long-term overall brightness change with a period of 7.2 years, i.e., basically the wide binary period, see Sect. 6. Bottom: independent rotational period determinations for suitable seasonal datasets. See text for details.

et al. 2017) (and also with its revised value of 2689±52 d by Aller et al. 2018). Orbital phase coherence of surface activity is common in comparably short period tidally-connected RS CVn binaries, but has never been seen for such long period timescales. Fig. 7 shows a comparison of the orbital radial velocities with our long-term APT photometry phased with the same orbital period of 2717 days from Jones et al. (2017). Most notable is the phase coherence in the sense that the light-curve maximum coincides with a time of highest radial velocity while the light-curve minimum coincides with a time of lowest radial velocity.

4.2. Rotational photometric modulation

Seasonal short period determinations are presented in the lower panel of Fig. 6. We note that the amplitude of the rotational modulation of IN Com is generally low, typically less than $0^{\mathrm{m}}1$ in *V*. Therefore, seasonal rotational periods were derived only for the best quality datasets with good phase coverage and low scatter. The average value of the seasonal periods is ≈5.92 days. At this point we emphasize that any photometric period always traces the rotation period of the star at that latitude where the spot or spots occurred. Interestingly, between 1995–1999, the photometric period was increasing, while the overall brightness was decreasing. Such a simultaneity is explained by surface differential rotation that causes a shift of the dominant longitude usually populated by star spots (cf. Vida et al. 2014).

Besides, our data again demonstrate the solidity of the 5.9-day photometric period being the rotation period as opposed to,
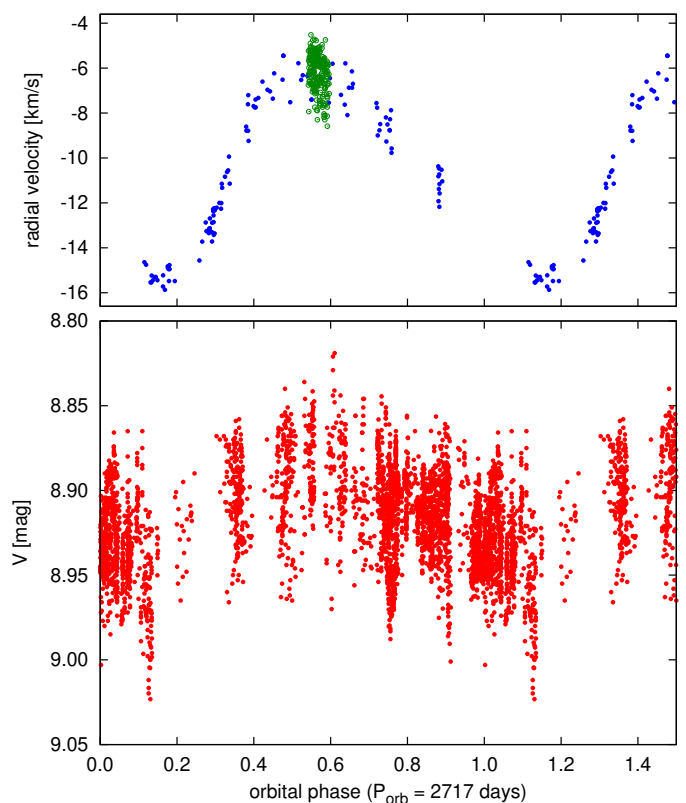

Fig. 7. Comparing the long-term light variation with the radial velocity curve of IN Com. Top: radial velocity curve of the star taken from Jones et al. (2017); suggesting a 2717-day long orbital period. Overplotted are the radial velocities from our spectroscopic data (green circles). Bottom: the long-term *V* + *y* photometric observations after folding up with the orbital period.

e.g., the 1.2-day ($1-f$) alias. This was already done in our Paper I but then we had not had a beautiful photometric light curve that sampled the variation with high-enough time resolution. Here we present two independent, densely sampled and time-continuous APT data (Fig. 8) that proof without doubt that the 5.9-day period is indeed the correct one.

The next step is to average the individual photometric period by applying a period search to the full data set. For this, we combine all the available high-precision *V* and *y* data into one single dataset and analyze it with the time-frequency analysis package MuFrAn. The resulting Fourier-amplitude spectrum is obtained for the pre-whitened data, that is the data with the long-term trend and the 2849-d period removed. The resulting amplitude spectrum is shown in the top panel of Fig. 9. Its highest peak suggests a long-term average photometric period of 5.934±0.001 d, which is very close to the average of the seasonal values. Consistently with the result of the differential rotation analysis in Sect. 5 this period is the apparent rotation period of the mid-latitude belt around ≈35° where spots cause the most significant light variation. Accordingly, in the bottom panel of Fig. 9, we fold the 30+ years of photometry with this period. It shows a phase coherency that is remarkable over that period of time. Thus, for future phase calculations, we suggest to use the following equation

$$\mathrm{HJD} = 2,449,415.0 + 5.934 \times E, \qquad (1)$$

where the reference time was taken from Paper I. This is also the ephemeris that we used to phased our Doppler images in Sect. 3.

Another finding is the frequency splitting of the dominant Fourier peak at 0.17 d^{-1}. The surrounding lower amplitude peaks are typical signature of differential surface rotation of the star (see the simulations in Strassmeier & Oláh 2004). Its individual peaks mark the stellar latitudes where the spots preferentially occurred. The five most prominent peaks of the Fourier-spectrum are listed in Table 3. Assuming that these peaks are due to surface differential rotation and the lowest and highest frequencies correspond to the polar and equatorial regions (or vice versa), we estimate a surface shear parameter of $\Delta P/P \approx 0.03$, albeit without any presumption on its sign. Such an estimation is usually erroneous, since the origin of the photometric signals is ambiguous (e.g., it is not known at which stellar latitudes the signaling spots are located). Nevertheless, this value is of the same order as we found from the cross-correlation analysis in Sect. 3.5 and confirms the existence of strong differential rotation on this G5 giant.

4.3. Radial velocity modulation

The top panel of Fig. 7 also shows the STELLA SES radial velocities from 2017. Note that a systematic zero point shift of 0.503 km s^{-1} was added to this data, see Strassmeier et al. (2012) for its determination with respect to the CORAVEL system. At this point we caution that the radial velocities in the Jones et al. (2017) paper differ in their zero point to same data re-plotted in the Aller et al. (2018) paper by ≈ 5 km s^{-1}. A zero point correction of -2.6 km s^{-1} should be applied for the Jones et al. (2017) data to satisfactorily fit our observations.

We first remove the grossly deviant velocities by a 3-σ filter (this removed 9 data points and left 214). The remaining SES velocities of IN Com have an internal precision of typically better than 2 km s^{-1}. A Fourier analysis shows a clean peak at $f \approx 0.17$, corresponding to a period of 5.95±0.03 d, but with an almost as strong $1 - f$ alias. Its full amplitude is almost 2 km s^{-1} but with

Fig. 9. Top: Fourier-amplitude spectrum for all the combined *V* and *y* photometric data shown in Fig. 6. Bottom: *V* and *y* data folded with $P_{\rm rot} = 5.934$ days.

an rms of the sinusoidal fit of the same order (Fig. 10). Nevertheless, we can now confirm our earlier suggestion that the low-amplitude radial velocity jitter of IN Com is spot modulated. Just recently, Aller et al. (2018) arrived at the same conclusion.

5. Characteristics of the Hα profiles

5.1. Line-profile morphology

Hα line profile variation is often associated with dynamo driven chromospheric activity, not seldom associated with a strong inhomogeneous stellar wind, coronal mass ejections and other violent events like flares. The most active stars have Hα in emission. Chromospheric, transition-region and coronal activity is indeed present in the case of IN Com as amply demonstrated by, e.g. strong Ca II H&K emission (see Paper 1), high-excitation UV lines like C IV (Modigliani et al. 1993) as well as strong X-ray emission (Montez et al. 2010). The overall Hα emission line profile appears permanently asymmetric which suggests intense long-lived mass motions at the upper chromosphere, giving some support to an origin related to an active binary system with mass
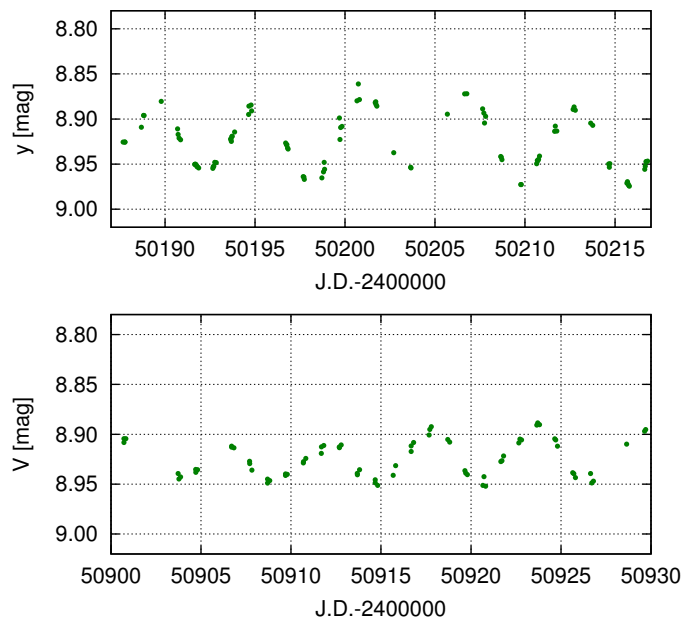

Fig. 8. Well sampled photometric modulation indicates the solidity of the 5.9-day period. Light curves were taken during April/May 1996 (top) and April 1998 (bottom) with the T7 and T6 APTs, respectively. The light curves even show the changing amplitudes and shapes typical for star spot evolution.
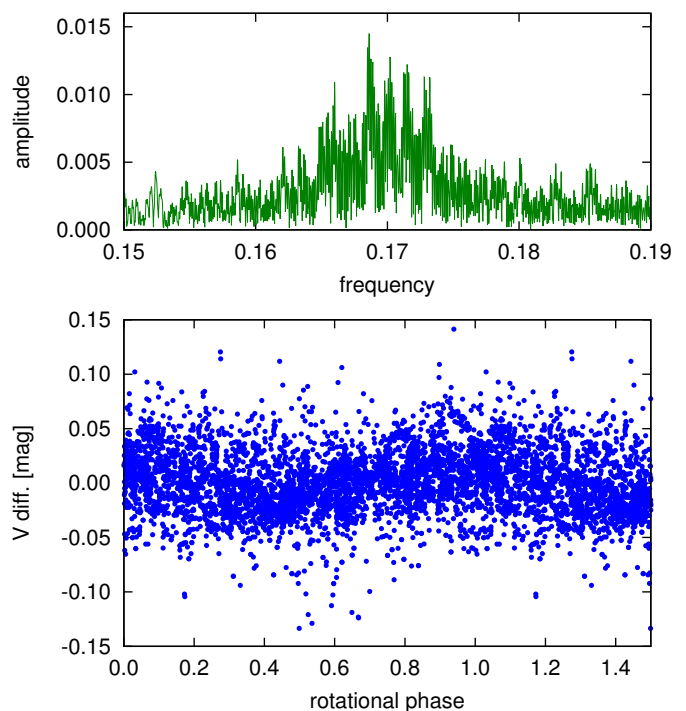
Table 3. The five most prominent periods and their wave amplitudes from the light curve Fourier-analysis.

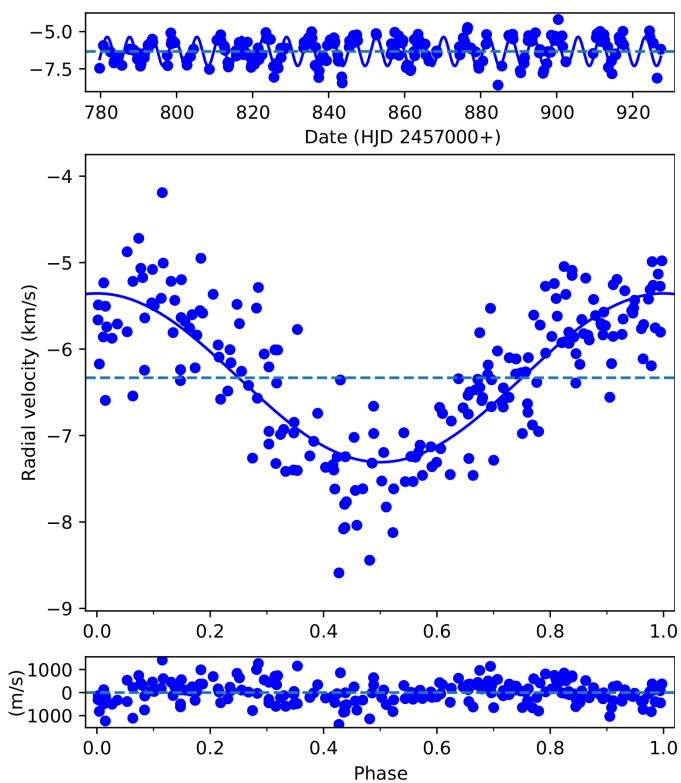| Frequency (1/d)	Amplitude (mag)	Period (d)
0.168506	0.0143	5.934
0.171509	0.0130	5.831
0.172930	0.0130	5.783
0.169810	0.0102	5.889
0.165874	0.0085	6.029

Fig. 10. Top: rotational modulation of the disk-integrated radial velocities of IN Com. Middle: the radial velocity measurements are phase folded with the rotation period and fitted with a sinusoidal. Bottom: residuals of the sinusoidal fit.

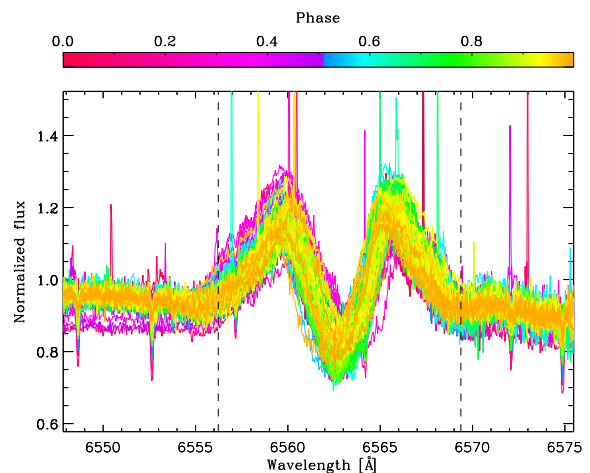**Fig. 11.** Overplot of the Hα SES spectra of IN Com from the first half of 2017. Indicated are the ± 300 km s^{-1} period-search limits imposed for the 2D FFT in Fig. 12.

same average width as the central Hα absorption. We measured FWHM for Hβ of 150 km s^{-1} and for Hγ of 160 km s^{-1}; however, unfortunately, Hβ falls at the edge of subsequent échelle-orders, while Hγ is significantly blended with a blue line at 4337.4 Å and therefore the S/N values for both lines are significanly lower compared with Hα; we estimate errors of 10-15 km s^{-1}. No emission above the continuum is seen neither for Hβ nor Hγ. We note that the width of the Hα absorption reversal is in agreement with the expected rotational broadening, and so are the absorption profiles of Hβ and Hγ.

5.2. Rotational modulation

To search for coherent temporal changes, we apply a 2D Fourier-periodogram to the Hα time series. It is based on a simple fast Fourier transform (FFT) analysis to each wavelength-calibrated pixel of the Hα profile within a velocity range of ± 300 km s^{-1} around the line center (for a more detailed description of the technique see Strassmeier et al. 2014). Note that one SES CCD pixel disperses ≈ 0.06 Å at Hα. The resulting 2D periodogram is shown in Fig. 12. It reveals a clear and dominating peak at $f = 0.169$ d^{-1} ($P = 5.92 \pm 0.06$ d), i.e., the expected rotation period of the giant. A second, much weaker peak is detected at $2f$ and is identified as its alias.

It is puzzling though that our 2D periodogram shows a gap with zero power for the 0.169 d^{-1} frequency in the red part of the line core just between zero and $\approx +70$ km s^{-1} velocity. We have no readily explanation for this.

5.3. Line shape and width

We compare the IN Com Hα profiles with the chromospheric and transition-region models put forward by Zboril et al. (2004). With their model 4 (Table 3 and Fig. 4 in Zboril et al. 2004), we find the overall best match for the average IN Com profile. We note that the match is not based on a rigorous line-profile fit but only on a qualitative comparison. The enormous width of the Hα emission of > 400 km s^{-1} had been presented as a puzzle (Aller et al. 2018) but is actually reproduced even with a normal plane-parallel atmosphere with an onset of the chromospheric temperature rise at around 5000 K at a (solar-like) mass depth of 1 g cm^{-2} and the assumption of complete frequency re-

motions. Thus, one would expect some rotational modulation of it if it is related to IN Com in the first place.

A time series of 208 Hα line profiles from the first half of 2017 is shown in Fig. 11. A broad emission profile with an average FWHM of ≈ 400 km s^{-1} (8.8 Å) superimposed with a central absorption reversal of width ≈ 150 km s^{-1} appears consistently throughout the time series. The line width at continuum exceeds the expected rotational width by a factor of ≈ 5. The rotational period and the equatorial rotational velocity give a radius of 11 R$_\odot$ (Table 1, adopting an inclination of 45° from Doppler imaging). If the Hα emission is bound to the star above FWHM would then suggest an origin of at least part of the emission at an extended radius, e.g. due to a circumstellar environment of up to 3–4 R$_\star$ (assuming corotation). This would mean that the overall Hα emission is composed of two parts; a chromospheric component and a circumstellar component. This has been seen and analyzed in several other (over)active stars, e.g. in UZ Librae (Zboril et al. 2004), FK Comae (Ramsey et al. 1981), II Pegasi (Short et al. 1998) and others, and is not a specific issue for IN Com because it is within a planetary nebula.

All three Balmer profiles of IN Com vary slightly and consistently from one observation to the next while its profile morphology remains basically unaltered over our entire observing season. No rotational modulation was detected so far although there are changes seen in Hα on a decade-long scale (Aller et al. 2018). The two pseudo emission peaks frequently reverse its relative strength in our data set; once the blue emission is stronger once the red emission is stronger. At this point we note that the Hβ and Hγ profiles of IN Com look vastly different than Hα. Both are purely in absorption with an asymmetric shape but of
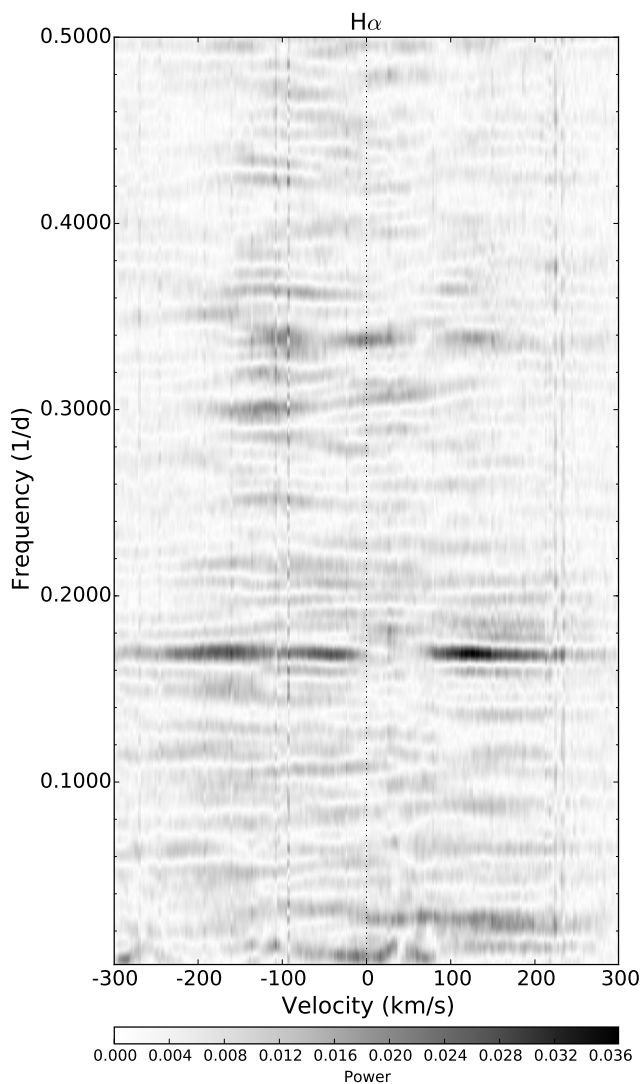
Fig. 12. Two-dimensional Fourier periodogram of the time series Hα profile from Fig. 11. Spectral power is indicated in gray-scale. The plot's horizontal range is ±300 km s⁻¹ around the line core while its vertical range is from 470 d at the bottom to 2 d at the top. The dominant excess power is detected at a frequency of ≈0.17, corresponding to a period of 5.92 d.

Fig. 13. Relationships between rotation and differential rotation for late-type single and binary stars. The position for IN Com is in agreement with the linear fit to (effectively) single stars, represented by the dotted line, suggesting that $|\alpha| \propto P_{\mathrm{rot}}[\mathrm{d}]/200$.

half of 2017 yielded 13 subsequent surface image reconstructions, which were used to estimate surface differential rotation. We found antisolar surface rotation profile with $\alpha = -0.026$ shear coefficient. This value falls within the recently proposed rotation-differential rotation relationship by Kővári et al. (2017), see Fig. 13. According to the plot, the linear fit for (effectively) single stars suggests $|\alpha| \propto P_{\mathrm{rot}}[\mathrm{d}]/200$. Moreover, the derived absolute surface shear of $\Delta\Omega = 0.027[\mathrm{rad/d}]$ would follow the general trend of $\Delta\Omega \propto T_{\mathrm{eff}}^p$ where $p = 5.8 \pm 1.0$ (see Fig. 2 in Kővári et al. 2017). Indeed, from the long-term photometric period variations we estimated the rate of the surface shear to be $\Delta P/P \approx 0.03$, which was in agreement with the shear coefficient derived from Doppler imaging.

The G-giant star in the center of the planetary nebula shows features originating from its evolutionary history. The giant is a barium-rich star; from our spectral synthesis (see Sect. 3.1) we estimate a [Ba/Fe] ratio of 0.85±0.25, supporting the former result of 0.50±0.30 by Thévenin & Jasniewicz (1997). We redetermined [Y/Fe] and [Sr/Fe] ratios as well, confirming the overabundance of these elements in the atmosphere of IN Com. The present configuration and the overabundant s-process elements of the G-star in the binary could be explained if the precursor of the white dwarf had originally the higher mass and therefore evolved faster to the white dwarf stage, while losing mass, and afterwards the companion (now G-star) was polluted by mass-transfer or wind accretion (cf. Verbunt & Phinney 1995).

The parallel variation of the long-term light curve with the orbital phase suggests a connection between the orbital motion of the binary and the activity of the G-giant. The star is the brightest and faintest at minimum and maximum radial velocity, respectively (see Sect. 4 Fig. 7).

We note finally that, although no observational evidence has been found so far to support the existence of accreting material around the G-star, its high angular momentum, the peculiar differential rotation, the Hα behaviour and the parallel variation of the long-term brightness with the orbital phase, may all be explained by the presence of an accretion disc tilted to the orbit.

distribution (CRD), which assumes that a photon absorbed in the wings is re-emitted in the core (see Avrett & Loeser 2003). The resulting Hα FWHM is of the order of 350 km s⁻¹ with a relative intensity of the emission peak of 1.2 and a 50% central self reversal. It implies an upper chromosphere with a temperature of 10,000 K and a logarithmic column density of −2.7 as well as a transition region (to the corona) with a temperature in excess of 100,000 K and a logarithmic column density of −6.

6. Summary and discussion

We have analyzed decade-long photometric and one season-long spectroscopic data of IN Com to derive more accurate stellar parameters and perform a time-series Doppler imaging study. From the long-term photometric observations we have confirmed a ≈5.973 day-long equatorial rotation period of the G-star. Also, we have provided more accurate astrophysical parameters for IN Com. Our time-series Doppler imaging study for the first
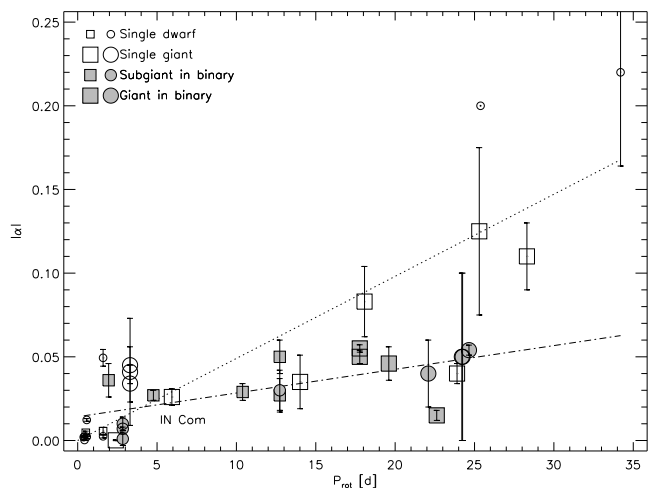
References

Aller, A., Lillo-Box, J., Vučković, M., et al. 2018, MNRAS, 476, 1140

Avrett, E. H. & Loeser, R. 2003, in IAU Symposium, Vol. 210, Modelling of Stellar Atmospheres, ed. N. Piskunov, W. W. Weiss, & D. F. Gray, A21

Bisterzo, S., Gallino, R., Straniero, O., Cristallo, S., & Käppeler, F. 2011, MNRAS, 418, 284

Carroll, T. A., Kopf, M., & Strassmeier, K. G. 2008, A&A, 488, 781

Carroll, T. A., Strassmeier, K. G., Rice, J. B., & Künstler, A. 2012, A&A, 548, A95

Castelli, F. & Kurucz, R. L. 2004, ArXiv Astrophysics e-prints

Ciardullo, R., Bond, H. E., Sipior, M. S., et al. 1999, AJ, 118, 488

Csubry, Z. & Kolláth, Z. 2004, in ESA Special Publication, Vol. 559, SOHO 14 Helio- and Asteroseismology: Towards a Golden Future, ed. D. Danesy, 396

De Marco, O., Bond, H. E., Harmer, D., & Fleming, A. J. 2004, ApJ, 602, L93

Donati, J.-F. & Collier Cameron, A. 1997, MNRAS, 291, 1

Feibelman, W. A. & Kaler, J. B. 1983, ApJ, 269, 592

Flower, P. J. 1996, ApJ, 469, 355

Gaia Collaboration, Brown, A. G. A., Vallenari, A., et al. 2018, ArXiv e-prints

González Martínez-País, I., Shahbaz, T., & Casares Velázquez, J. 2014, Accretion Processes in Astrophysics

Granzer, T., Reegen, P., & Strassmeier, K. G. 2001, Astronomische Nachrichten, 322, 325

Gray, D. F. 1981, ApJ, 251, 155

Gray, D. F. & Toner, C. G. 1986, ApJ, 310, 277

Guerrero, M. A. 2012, in IAU Symposium, Vol. 283, IAU Symposium, 204–210

Gustafsson, B., Edvardsson, B., Eriksson, K., et al. 2008, A&A, 486, 951

Jasniewicz, G., Acker, A., & Duquennoy, A. 1987, A&A, 180, 145

Jasniewicz, G., Acker, A., Mauron, N., Duquennoy, A., & Cuypers, J. 1994, A&A, 286, 211

Jasniewicz, G., Thevenin, F., Monier, R., & Skiff, B. A. 1996, A&A, 307, 200

Jones, D. & Boffin, H. M. J. 2017, Nature Astronomy, 1, 0117

Jones, D., Van Winckel, H., Aller, A., Exter, K., & De Marco, O. 2017, A&A, 600, L9

Kővári, Zs., Kriskovics, L., Künstler, A., et al. 2015, A&A, 573, A98

Kővári, Zs., Oláh, K., Kriskovics, L., et al. 2017, Astronomische Nachrichten, 338, 903

Kuczawska, E. & Mikolajewski, M. 1993, Acta Astron., 43, 445

Künstler, A., Carroll, T. A., & Strassmeier, K. G. 2015, A&A, 578, A101

Kupka, F., Piskunov, N., Ryabchikova, T. A., Stempels, H. C., & Weiss, W. W. 1999, A&AS, 138, 119

Lindborg, M., Hackman, T., Mantere, M. J., et al. 2014, A&A, 562, A139

Longmore, A. J. & Tritton, S. B. 1980, MNRAS, 193, 521

Malasan, H. L., Yamasaki, A., & Kondo, M. 1991, AJ, 101, 2131

Montez, Jr., R., De Marco, O., Kastner, J. H., & Chu, Y.-H. 2010, ApJ, 721, 1820

Noskova, R. I. 1989, Soviet Astronomy Letters, 15, 149

Paczyński, B. 1976, in IAU Symposium, Vol. 73, Structure and Evolution of Close Binary Systems, ed. P. Eggleton, S. Mitton, & J. Whelan, 75

Piskunov, N. & Valenti, J. A. 2017, A&A, 597, A16

Podsiadlowski, P. 2001, in Astronomical Society of the Pacific Conference Series, Vol. 229, Evolution of Binary and Multiple Star Systems, ed. P. Podsiadlowski, S. Rappaport, A. R. King, F. D'Antona, & L. Burderi, 239

Pojmanski, G. 2002, Acta Astron., 52, 397

Ramsey, L. W., Nations, H. L., & Barden, S. C. 1981, ApJ, 251, L101

Short, C. I., Byrne, P. B., & Panagi, P. M. 1998, A&A, 338, 191

Strassmeier, K. G., Boyd, L. J., Epand, D. H., & Granzer, T. 1997a, PASP, 109, 697

Strassmeier, K. G., Granzer, T., Weber, M., et al. 2010, Advances in Astronomy, 2010, 19

Strassmeier, K. G., Hubl, B., & Rice, J. B. 1997b, A&A, 322, 511

Strassmeier, K. G., Ilyin, I., Järvinen, A., et al. 2015, Astronomische Nachrichten, 336, 324

Strassmeier, K. G., Ilyin, I., & Steffen, M. 2018, A&A, 612, A44

Strassmeier, K. G. & Oláh, K. 2004, in ESA Special Publication, Vol. 538, Stellar Structure and Habitable Planet Finding, ed. F. Favata, S. Aigrain, & A. Wilson, 149–161

Strassmeier, K. G., Weber, M., Granzer, T., & Järvinen, S. 2012, Astronomische Nachrichten, 333, 663

Strassmeier, K. G., Weber, M., Granzer, T., et al. 2014, Astronomische Nachrichten, 335, 904

Thévenin, F. & Jasniewicz, G. 1997, A&A, 320, 913

Tout, C. A. & Regős, E. 2003, in Astronomical Society of the Pacific Conference Series, Vol. 293, 3D Stellar Evolution, ed. S. Turcotte, S. C. Keller, & R. M. Cavallo, 100

Van Winckel, H., Jorissen, A., Exter, K., et al. 2014, A&A, 563, L10

Verbunt, F. & Phinney, E. S. 1995, A&A, 296, 709

Vida, K., Oláh, K., & Szabó, R. 2014, MNRAS, 441, 2744

Weber, M., Granzer, T., & Strassmeier, K. G. 2012, in Society of Photo-Optical Instrumentation Engineers (SPIE) Conference Series, Vol. 8451, Society of Photo-Optical Instrumentation Engineers (SPIE) Conference Series, 0

Weber, M., Granzer, T., Strassmeier, K. G., & Woche, M. 2008, in Society of Photo-Optical Instrumentation Engineers (SPIE) Conference Series, Vol. 7019, Society of Photo-Optical Instrumentation Engineers (SPIE) Conference Series, 0

Weber, M. & Strassmeier, K. G. 2011, A&A, 531, A89

Zboril, M., Strassmeier, K. G., & Avrett, E. H. 2004, A&A, 421, 295

Appendix A: Log of spectroscopic data

Table A.1. Observing log of STELLA-SES spectra of IN Com from 2017 used for individual Doppler reconstructions shown in Sect. 3

HJD[a]	Phase[b]	Date	S/N	Subset
7780.746	0.799	27.01.2017	102	S01
7782.600	0.111	29.01.2017	184	S01
7783.521	0.266	29.01.2017	149	S01
7783.676	0.292	30.01.2017	170	S01
7784.611	0.450	31.01.2017	160	S01
7785.603	0.617	01.02.2017	140	S01
7787.503	0.937	02.02.2017	144	S01
7787.656	0.963	03.02.2017	176	S01
7788.653	0.131	04.02.2017	166	S02
7789.502	0.274	04.02.2017	135	S02
7790.496	0.442	05.02.2017	144	S02
7790.617	0.462	06.02.2017	195	S02
7791.498	0.611	06.02.2017	143	S02
7791.618	0.631	07.02.2017	185	S02
7792.498	0.779	07.02.2017	147	S02
7792.619	0.800	08.02.2017	185	S02
7793.499	0.948	08.02.2017	169	S02
7793.620	0.968	09.02.2017	197	S02
7793.744	0.989	09.02.2017	188	S02
7808.623	0.497	24.02.2017	186	S03
7811.607	0.999	27.02.2017	178	S03
7811.730	0.020	27.02.2017	168	S03
7812.494	0.149	27.02.2017	175	S03
7812.618	0.170	28.02.2017	193	S03
7812.738	0.190	28.02.2017	174	S03
7813.490	0.317	28.02.2017	177	S03
7813.612	0.337	01.03.2017	198	S03
7813.733	0.358	01.03.2017	186	S03
7815.593	0.671	03.03.2017	191	S03
7815.715	0.692	03.03.2017	137	S03
7816.486	0.822	03.03.2017	154	S03
7816.607	0.842	04.03.2017	184	S03
7817.506	0.994	04.03.2017	105	S04
7817.628	0.014	05.03.2017	110	S04
7818.495	0.160	05.03.2017	153	S04
7818.616	0.181	06.03.2017	123	S04
7819.431	0.318	06.03.2017	118	S04
7819.599	0.346	07.03.2017	181	S04
7819.720	0.367	07.03.2017	134	S04
7820.481	0.495	07.03.2017	108	S04
7821.547	0.675	09.03.2017	116	S04
7821.668	0.695	09.03.2017	142	S04
7822.473	0.831	09.03.2017	101	S04
7823.490	0.002	10.03.2017	177	S05
7823.603	0.021	11.03.2017	132	S05
7824.491	0.171	11.03.2017	166	S05
7824.694	0.205	12.03.2017	90	S05
7825.490	0.339	12.03.2017	169	S05
7825.615	0.360	13.03.2017	119	S05
7826.397	0.492	13.03.2017	117	S05
7826.521	0.513	13.03.2017	156	S05
7826.711	0.545	14.03.2017	173	S05

HJD[a]	Phase[b]	Date	S/N	Subset
7827.397	0.660	14.03.2017	122	S05
7827.520	0.681	14.03.2017	184	S05
7828.391	0.828	15.03.2017	97	S05
7828.720	0.883	16.03.2017	165	S05
7833.669	0.717	21.03.2017	164	S06
7834.401	0.841	21.03.2017	144	S06
7834.521	0.861	21.03.2017	178	S06
7834.676	0.887	22.03.2017	147	S06
7835.524	0.030	22.03.2017	143	S06
7835.644	0.050	23.03.2017	146	S06
7836.696	0.228	24.03.2017	145	S06
7837.524	0.367	24.03.2017	175	S06
7838.401	0.515	25.03.2017	167	S06
7838.523	0.535	25.03.2017	183	S07
7839.432	0.689	26.03.2017	88	S07
7840.402	0.852	27.03.2017	168	S07
7840.525	0.873	27.03.2017	169	S07
7840.647	0.893	28.03.2017	171	S07
7841.404	0.021	28.03.2017	155	S07
7841.527	0.042	28.03.2017	178	S07
7841.651	0.062	29.03.2017	169	S07
7842.404	0.189	29.03.2017	159	S07
7842.525	0.210	29.03.2017	169	S07
7842.646	0.230	30.03.2017	130	S07
7843.440	0.364	30.03.2017	148	S07
7843.573	0.386	31.03.2017	91	S07
7860.400	0.222	16.04.2017	164	S08
7861.400	0.391	17.04.2017	173	S08
7861.645	0.432	18.04.2017	161	S08
7863.401	0.728	19.04.2017	164	S08
7864.401	0.896	20.04.2017	87	S08
7864.650	0.938	21.04.2017	149	S08
7865.623	0.102	22.04.2017	146	S08
7868.403	0.571	24.04.2017	186	S08
7868.566	0.598	25.04.2017	163	S08
7874.406	0.582	30.04.2017	180	S09
7874.526	0.603	30.04.2017	159	S09
7874.699	0.632	01.05.2017	120	S09
7875.406	0.751	01.05.2017	171	S09
7876.450	0.927	02.05.2017	159	S09
7877.531	0.109	03.05.2017	141	S09
7879.404	0.425	05.05.2017	170	S09
7879.525	0.445	05.05.2017	167	S09
7884.555	0.293	11.05.2017	92	S09
7890.413	0.280	16.05.2017	112	S10
7890.534	0.300	17.05.2017	128	S10
7891.414	0.449	17.05.2017	150	S10
7891.534	0.469	18.05.2017	150	S10
7892.484	0.629	18.05.2017	148	S10
7892.606	0.650	19.05.2017	120	S10
7893.414	0.786	19.05.2017	142	S10
7893.535	0.806	20.05.2017	162	S10
7894.415	0.954	20.05.2017	107	S10
7895.415	0.123	21.05.2017	122	S10
7895.627	0.159	22.05.2017	123	S10
7896.415	0.291	22.05.2017	113	S11
7896.604	0.323	23.05.2017	154	S11

HJD[a]	Phase[b]	Date	S/N	Subset
7897.601	0.491	24.05.2017	136	S11
7898.598	0.659	25.05.2017	148	S11
7899.417	0.797	25.05.2017	92	S11
7899.597	0.828	26.05.2017	140	S11
7900.613	0.999	27.05.2017	78	S11
7901.590	0.163	28.05.2017	144	S11
7910.418	0.651	05.06.2017	170	S12
7910.584	0.679	06.06.2017	127	S12
7911.418	0.820	06.06.2017	139	S12
7911.549	0.842	07.06.2017	123	S12
7912.610	0.021	08.06.2017	95	S12
7913.419	0.157	08.06.2017	171	S12
7914.419	0.325	09.06.2017	173	S12
7914.550	0.347	10.06.2017	130	S12
7915.553	0.517	11.06.2017	106	S12

[a] 2 450 000+
[b] Phases computed using Eq. 1.

Table A.2. Observing log of PEPSI@VATT spectra of IN Com from March 2017

HJD[a]	Phase[b]	Date	S/N$_{III}$[c]	S/N$_V$[d]
7819.804	0.381	07.03.2017	50	80
7819.959	0.407	07.03.2017	42	73
7820.847	0.557	08.03.2017	31	82
7820.990	0.581	08.03.2017	41	94
7821.804	0.718	09.03.2017	54	96
7821.963	0.745	09.03.2017	45	103
7822.779	0.882	10.03.2017	45	97
7822.958	0.912	10.03.2017	50	94
7823.838	0.061	11.03.2017	38	97
7824.008	0.089	11.03.2017	22	60
7824.792	0.221	12.03.2017	39	97
7824.986	0.254	12.03.2017	36	89
7825.798	0.391	13.03.2017	45	88
7826.003	0.425	13.03.2017	48	83
7826.799	0.560	14.03.2017	41	104
7826.994	0.593	14.03.2017	53	104
7827.792	0.727	15.03.2017	48	90
7827.945	0.753	15.03.2017	47	85

[a] $2\,450\,000+$
[b] Phases computed using Eq. 1.
[c] Signal-to-noise ratio using CD III (blue) cross-disperser
[d] Signal-to-noise ratio using CD V (red) cross-disperser
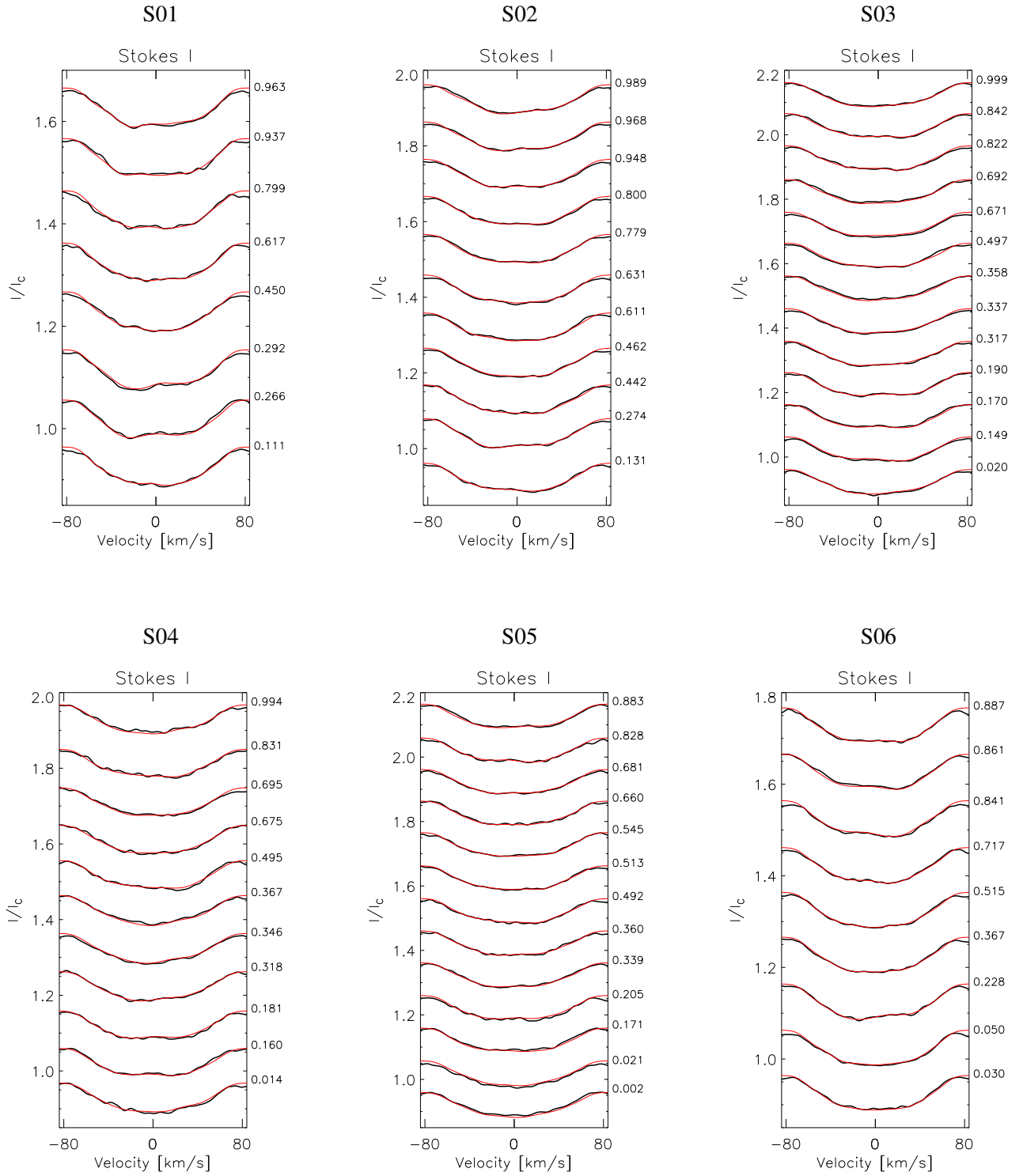
Fig. A.1. Observed line profiles (thick black lines) and their model fits (thin red lines) for the Doppler reconstructions S01-S06 shown in Fig. 1. The phases of the individual observations are listed on the right side of the panels.
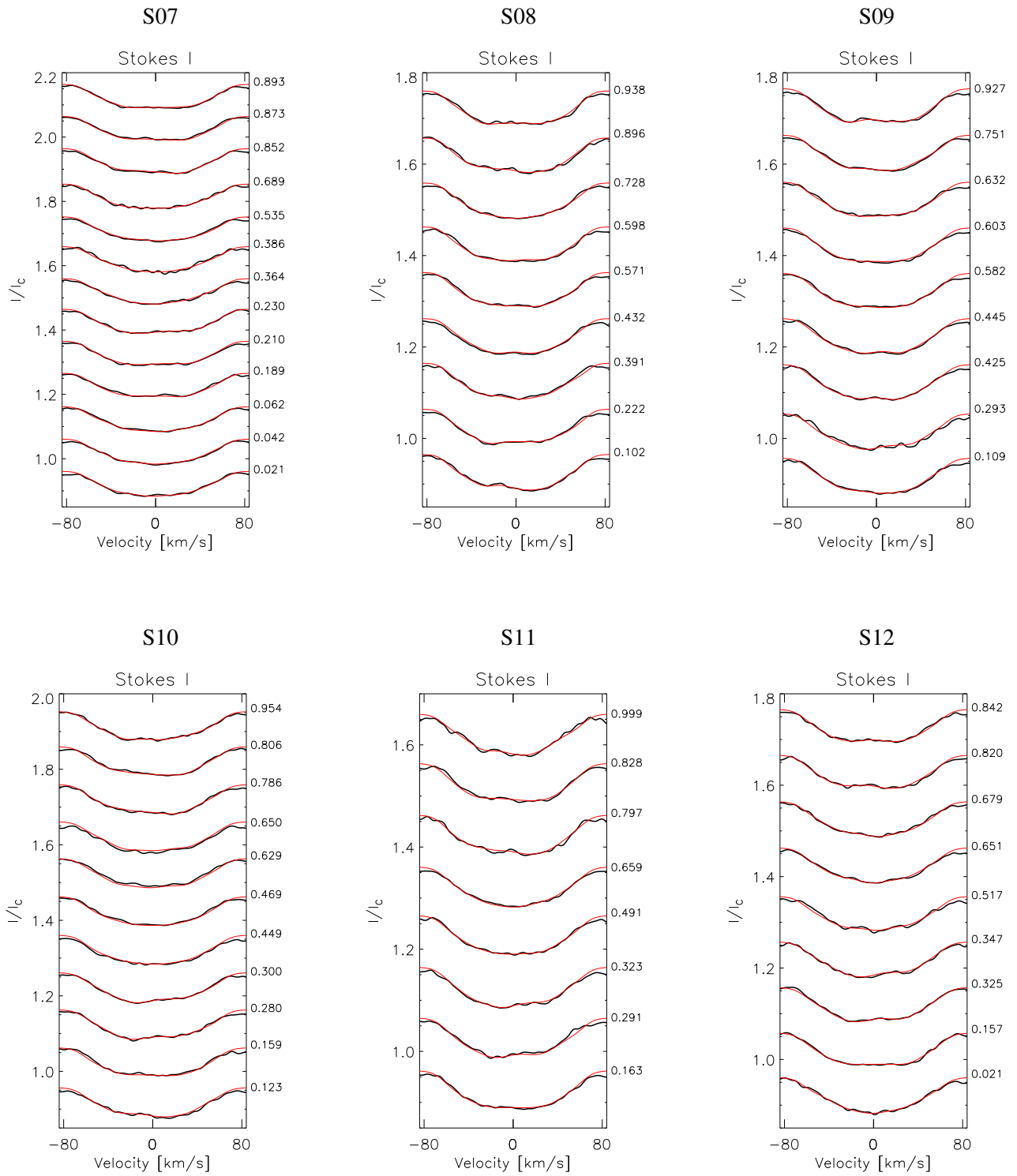
Fig. A.2. Observed line profiles (thick black lines) and their model fits (thin red lines) for the Doppler reconstructions S07-S12 shown in Fig. 2. The phases of the individual observations are listed on the right side of the panels.
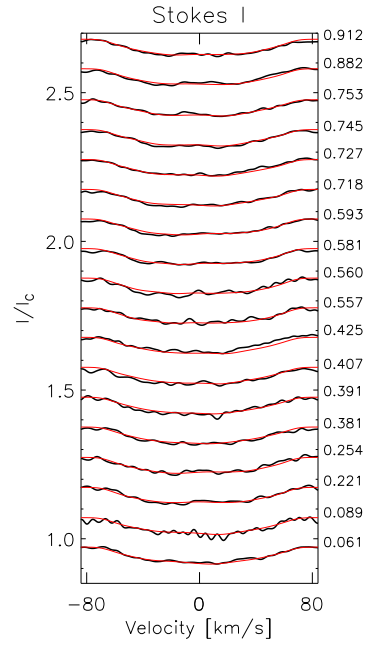
Fig. A.3. Observed line profiles (thick black lines) and their model fits (thin red lines) for the Doppler reconstruction applied for the PEPSI@VATT spectra shown in Fig. 3. The phases of the individual observations are listed on the right side of the panel.